

Present day climate forcing and response from black carbon in snow

Mark G. Flanner, Charles S. Zender, James T. Randerson

Department of Earth System Science, University of California at Irvine

Philip J. Rasch

National Center for Atmospheric Research, Boulder, CO

Abstract. We apply our SNow, ICe, and Aerosol Radiative (SNICAR) model, coupled to a GCM with prognostic carbon aerosol transport to improve understanding of climate forcing and response from black carbon (BC) in snow. Building on two previous studies, we account for interannually-varying biomass burning BC emissions, snow aging, and aerosol scavenging by snow meltwater. We assess uncertainty in forcing estimates from these factors, as well as BC optical properties and snow cover fraction. BC emissions are the largest source of uncertainty, followed by snow aging. The rate of snow aging determines snowpack effective radius (r_e), which directly controls snow reflectance and the magnitude of albedo change caused by BC. For a reasonable r_e range, reflectance reduction from BC varies three-fold. Inefficient meltwater scavenging keeps hydrophobic impurities near the surface during melt and enhances forcing. Applying biomass burning BC emission inventories for a strong (1998) and weak (2001) boreal fire year, we estimate global annual mean BC/snow surface radiative forcing from all sources (fossil fuel, biofuel, and biomass burning) of $+0.054$ (0.007 – 0.13) and $+0.049$ (0.007 – 0.12) W m^{-2} , respectively. Snow forcing from only fossil fuel+biofuel sources is $+0.043$ W m^{-2} (forcing from only fossil fuels is $+0.033$ W m^{-2}), suggesting the anthropogenic contribution to total forcing is at least 80%. 1998 global land and sea-ice snowpack absorbed 0.60 and 0.23 W m^{-2} , respectively, because of direct BC/snow forcing. The forcing is maximum coincidentally with snowmelt onset, triggering strong snow-albedo feedback in local springtime. Consequently, the “efficacy” of BC/snow forcing is more than 3 times greater than forcing by CO_2 . 1998 and 2001 land snowmelt rates north of 50°N are 28% and 19% greater in the month preceding maximum melt of control simulations without BC in snow. With climate feedbacks, global annual mean 2-meter air temperature warms 0.15 and 0.10°C , when BC is included in snow, whereas annual arctic warming is 1.61 and 0.50°C . Stronger high-latitude climate response in 1998 than 2001 is at least partially caused by boreal fires, which account for nearly all of the 35% biomass burning contribution to 1998 arctic forcing. Efficacy was anomalously large in this experiment, however, and more research is required to elucidate the role of boreal fires, which we suggest have maximum arctic BC/snow forcing potential during April–June. Model BC concentrations in snow agree reasonably well ($r = 0.78$) with a set of 23 observations from various locations, spanning nearly 4 orders of magnitude. We predict concentrations in excess of 1000 ng g^{-1} for snow in northeast China, enough to lower snow albedo by more than 0.13 . The greatest instantaneous forcing is over the Tibetan Plateau, exceeding 20 W m^{-2} in some places during spring. These results indicate that snow darkening is an important component of carbon aerosol climate forcing.

1. Introduction

Very small quantities of black carbon (BC, the strongly absorbing component of carbonaceous aerosols) reduce snow reflectance because of multiple scattering in the snowpack and huge disparity between mass absorption coefficients of BC and ice [e.g., ?]. Reflectance reduction caused by BC and other absorbing impurities is of concern because slight changes in solar absorption can alter snowmelt timing, and snow spatial coverage is tightly coupled to climate through snow-albedo feedback [e.g., ?].

Several other positive feedbacks amplify the first-order warming effect of BC in snow. Warmer snow temperatures can accelerate snow effective radius (r_e) growth [e.g., ?], which darkens the snow itself. Second, the radiative perturbation of a given BC mass

mixing ratio is greater in snow with larger r_e [?]. Third, spring and summer melting can concentrate hydrophobic and large impurities near the snow surface [?]. Fourth, the stable atmosphere of high latitudes prevents rapid heat exchange with the upper troposphere, resulting in strong surface temperature response to surface radiative forcings [?]. We represent all of these feedbacks with a coupled snow-aerosol-climate model.

? raised awareness of BC/snow forcing by assuming spatially-uniform snow albedo reductions over arctic sea-ice and northern hemisphere land. They estimate global adjusted BC/snow radiative forcing of $+0.15$ W m^{-2} , and global warming of 0.24°C , yielding a forcing “efficacy” [?], or change in equilibrium global mean temperature per unit power of radiative forcing, double that of CO_2 . ? scaled the BC/snow forcing based on deposition fields and revised their original estimate to $+0.05$ W m^{-2} (corrected value published in Appendix A.5 of ?), with a warming of 0.065°C . ? predicts snow and ice reflectance with a radiative transfer solution that interactively depends on BC deposition in an aerosol/chemical transport GCM. He predicts warming of 0.06°C from snow darkening by fossil fuel and biofuel BC.

We attempt to build upon these studies by accounting for, and assessing uncertainty from interannually-varying biomass burning BC emissions, snow aging and spatially-varying grain size, melt-water scavenging of BC in the snowpack, BC optical properties, and snow cover fraction. We discuss some features of our SNow, ICe, and Aerosol Radiative (SNICAR) model, including the influence of snow r_e on reflectance and vertical heating perturbation from BC. Next we compare global predictions of BC in snow with observations. Then we estimate the global climate response and efficacy of BC/snow forcing, finding three-fold greater global temperature response than expected from equal forcing by CO_2 . Finally, we look at spatial and temporal patterns of the forcing and climate response with the goal of understanding this large efficacy in the context of snowmelt timing and snow-albedo feedback.

2. Methods

We simulate radiative transfer in the snowpack with SNICAR [?], which utilizes theory from ? and the two-stream, multi-layer radiative approximation of ?. The multi-layer model allows for vertically-heterogeneous snow properties and heating, and influence of surfaces underlying snowpack. We couple this snow radiative model to the National Center for Atmospheric Research (NCAR) Community Atmosphere Model, version 3 (CAM3) [e.g., ?], with configuration described below.

Hemispheric radiative fluxes may be accurately estimated for media composed of aspherical ice particles by assuming collections of spheres that conserve the total surface area and volume of the real media [???]. For this reason, r_e , or surface area-weighted mean radius, is the most appropriate snow grain metric for optical considerations. We compute Mie parameters offline at fine spectral resolution for lognormal distributions of absorbing aerosols and a wide range of ice r_e . Coupled to a GCM, SNICAR uses only 5 spectral bands (0.3 – 0.7, 0.7 – 1.0, 1.0 – 1.2, 1.2 – 1.5, and 1.5 – 5.0 μm) for computational efficiency. Following the Chandrasekhar Mean approach, optical properties are weighted into broad bands according to incident solar flux [?]. We use surface incident flux typical of mid-latitude winter for clear- and cloudy-sky conditions, generated with the atmospheric ShortWave Narrow-Band Model (SWNB) [?]. In addition to weighting by solar flux, we also weight single-scatter albedo (ω) for ice grains by hemispheric albedo of an optically-thick snowpack:

$$\omega(\bar{\lambda}) = \frac{\int_{\lambda_1}^{\lambda_2} \omega(\lambda) S_s^{\downarrow}(\lambda) \alpha(\lambda) d\lambda}{\int_{\lambda_1}^{\lambda_2} S_s^{\downarrow}(\lambda) \alpha(\lambda) d\lambda} \quad (1)$$

where S_s^{\downarrow} is the downwelling surface incident flux (unique for diffuse and direct cases), and α is the hemispheric albedo of an optically-thick snowpack of homogeneous r_e .

This weighting scheme produces relative error in albedo predicted using 5 bands of less than 0.5%, relative to 470-band solutions. Over a wide range of zenith angles, effective radii, and impurity concentrations, we found this technique to be significantly more accurate (factor of five difference in mean relative error) in predicting spectrally-averaged albedo than when ω is weighted only by S_s^{\downarrow} . However, we stress that it is only an empirical approach and provides undesirable results in more general cases (such as the case of weighting the limits $\omega = 0$ and $\omega = 1$). It also requires *a priori* narrowband albedo values of the bulk medium. Errors in sub-2 cm absorption with this approach are $\sim 4\%$, slightly greater than errors without the albedo weighting of ω . Broadband Mie parameters for $50 \leq r_e \leq 1000 \mu\text{m}$ are compiled into a lookup table for online retrieval in the host GCM.

We partition online surface-incident visible and near-infrared (NIR), diffuse and direct flux into the 5 bands used by SNICAR using the same offline estimates of narrowband mid-latitude winter fluxes. We apply the delta-Eddington [?] and delta-Hemispheric Mean [?] approximations in the visible and NIR spectra, respectively. In very rare situations (about 1 in 10^6 cases), the multi-layer

solution approaches an indeterminate case with direct-beam incident flux [?] so we adjust the sun angle by a few degrees to achieve reasonable predictions.

Multiple aerosol species are accounted for by summing extinction optical depths of each component, weighting individual single-scatter albedos by optical depths, and weighting asymmetry parameters by the product of optical depths and single-scatter albedos. Hydrophilic and hydrophobic BC species are treated separately. Absolute error in albedo predicted with 5 bands for snow with BC is also $< 0.5\%$, although albedo reduction from typical BC concentrations is consistently 4 – 6% (relative) less with 5 bands than with 470. As we will show, this bias is much smaller than other uncertainties.

We couple SNICAR to the CAM3 GCM with a slab ocean model that has spatially-varying mixed layer depth with fixed monthly-mean ocean heat transport. We include prognostic transport and wet and dry deposition of hydrophobic and hydrophilic BC and organic carbon (OC) [?], using a single size bin for each of these four components. Wet deposition tendencies consist of both first-order loss from below-cloud scavenging by precipitation and in-cloud scavenging that assumes a fixed fraction of aerosol resides within the cloud water. BC and OC dry deposition velocities are fixed at 1 mm s^{-1} [e.g., ?]. Carbon aerosols are emitted into the atmosphere as hydrophobic and then transform to hydrophilic components with an e-folding time of 1.2 days. Transformation ceases upon deposition to the snowpack.

Snow on land is represented in the Community Land Model (CLM3) [e.g., ?] with a 5-layer model based on ? that accounts for vertically-resolved snow thermal processes, densification, and meltwater transport. Snow on sea-ice is represented with a single layer in the Community Sea Ice Model (CSIM) component of CAM3. Radiative layers in SNICAR match thermal layers in these models. GCM gridcell area is approximately 97000 km^2 near the equator and 17600 km^2 at 80°N .

We calculate instantaneous radiative forcing of carbon aerosols in both snow and the atmosphere at each radiative transfer timestep as the difference in absorbed radiation with all aerosols and all aerosols except carbon aerosols. Radiative transfer estimates with carbon aerosols feed back into the model climate. Reported atmospheric forcings are from BC+OC, whereas snow forcings are from only BC (discussed below).

Forcing is sensitive to cloud treatment, which strongly affects both surface-incident and outgoing top-of-atmosphere radiative fluxes. Cloud fraction is diagnosed based on relative humidity,

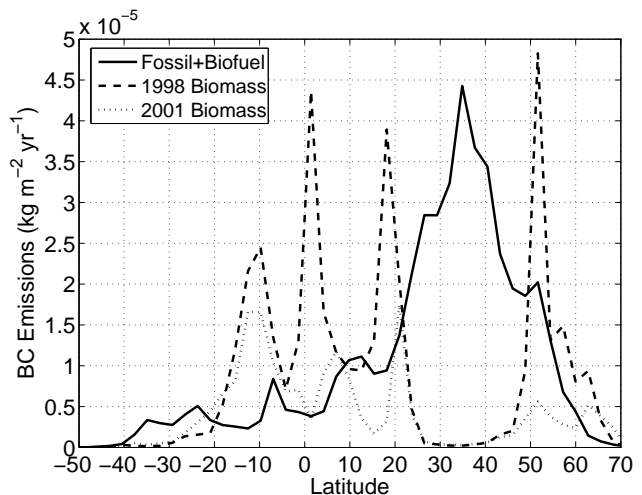


Figure 1. Zonal annual mean black carbon emissions from fossil fuel+biofuel combustion [?] and biomass burning during 1998 and 2001 [?].

Table 1. Configurations for 1998 and 2001 Low, Central, and High Experiments

	Low Estimate	Central Estimate	High Estimate
FF+BF BC Emissions [Tg yr^{-1}] (Global/N of 30°N)	1.6/1.0	4.7/2.7	16.2/9.3
1998 BB BC Emissions [Tg yr^{-1}] (Global/N of 30°N)	2.1/0.4	4.1/0.8	6.5/1.6
2001 BB BC Emissions [Tg yr^{-1}] (Global/N of 30°N)	1.1/0.1	2.0/0.2	3.0/0.4
BC MAC (fresh, hydrophobic) [$\text{m}^2 \text{g}^{-1}$ at 550 nm]	6.3	7.5	8.7
BC MAC (aged, hydrophilic) [$\text{m}^2 \text{g}^{-1}$ at 550 nm]	9.5	11.3	13.1
Snow Aging Scaling Factor	0.5	1.0	2.0
Snow Cover Fraction	?	?	?
Hydrophilic Meltwater Scavenging Ratio (k_{phi})	2.0	0.2	0.02
Hydrophobic Meltwater Scavenging Ratio (k_{pho})	0.3	0.03	0.003

atmospheric stability, and convective mass fluxes [?]. The cloud vertical overlap parameterization is described in ?. Liquid and ice cloud optical properties are parameterized according to ? and ?, respectively. Thus mixed-phase bulk cloud radiative properties depend on prognosed cloud water path [e.g., ?], temperature-dependent drop effective radius, and ice fraction. Liquid and ice hydrometeors are each represented with a single size category. Finally, the atmospheric multi-layer radiative transfer approximation [?] utilizes the delta-Eddington approximation and 19 spectral bands in the solar spectrum. Atmospheric and snow radiative transfer are solved separately for practical reasons, as the atmospheric radiation model is engineered to utilize pre-determined surface albedo.

To estimate present-day global forcing of BC in snow, we consider combinations of low, central, and high estimates of the following factors:

2.1. BC and OC Emissions

We use low, central, and high fossil fuel (FF) and biofuel (BF), BC and OC emission estimates at $1^\circ \times 1^\circ$ resolution from ?. These annual mean estimates are derived from 1996 fuel-use data and assumptions about local combustion technology and practice. We use monthly biomass burning (BB) estimates of BC and OC from the Global Fire Emissions Database, version 2 (GFEDv2) [?], which are derived from satellite-monitored burned area, modeled fuel load and combustion completeness, and aerosol emission factors from ?, personal communication. We also apply regional satellite-derived carbon monoxide inversion factors (*Prasad Kasibhatla, unpublished data, 2006*), which constrain the forward emission estimates. Boreal forest fires exhibit strong interannual variability and are likely the dominant source of arctic BC during moderate fire seasons [?]. In this 1997–2004 BB emissions timeseries, 1998 was the strongest boreal fire year, and we select 2001 as representative of a weak year. Boreal emissions were weaker in 1997, but global emissions were greatest this year. We estimate high and low emissions at each gridcell and month for these two years by combining standard error, in quadrature, of regional CO inversion factors, and CO and BC emission factors [?, personal communication]. Assuming a broad range of emissions may compensate for some variability in atmospheric transport mechanisms, which we do not address here. Zonal-mean, annual FF+BF and BB emissions are shown in Figure 1, where a large difference in high-latitude BB emissions between 1998 and 2001 can be seen. Table 1 lists global and boreal annual FF+BF and BB emission estimates, and all other experimental configurations.

All emissions enter the lowest model atmosphere layer. Particulate matter from strong fires can be injected above the boundary layer however, and assumptions about injection height may affect model high-latitude upper troposphere heating [?]. Lacking associated injection height information for our emission inventories, we do not assess forcing sensitivity to this factor.

2.2. Optical Properties

? comprehensively review current understanding of optical properties of freshly-combusted light absorbing aerosols. They suggest a mass absorption cross section (MAC) of $7.5 \pm 1.2 \text{ m}^2 \text{ g}^{-1}$ at $\lambda = 550 \text{ nm}$ for uncoated particles, based mostly on samples

from diesel engines and traffic tunnels. Particle density, refractive index, size distribution, coatings, and morphology all affect the optical properties. But current understanding of these physical parameters, combined with Mie or Rayleigh-Debye-Gans theory, underpredict observed MAC by $\sim 30\%$ [?]. Commonly used optical properties [?] are in the correct observational range of BC MAC, but are derived by applying Mie theory to a highly unrealistic combination of physical properties. Scattering magnitude and direction by realistic BC concentrations have negligible effect on bulk snowpack radiative transfer because scattering is dominated by the ice crystals. Therefore, realistic BC MAC, even if derived with assumptions that produce unrealistic ω and scattering phase function, predicts realistic snowpack absorption enhancement. (This is not necessarily true for absorbing aerosols in the atmosphere, where scattering optical depth is much lower). For hydrophobic BC, we use indices of refraction from ?, number-median radius of $0.05 \mu\text{m}$ (a central value among many studies published in ?), and lognormal size distribution with geometric standard deviation of 1.5. We use particle density as a tuning parameter to obtain $\text{MAC} = 7.5 \text{ m}^2 \text{ g}^{-1}$ (\pm one standard deviation from ? for low and high estimates) at $\lambda = 550 \text{ nm}$.

Coagulation between BC particles and collapse of the aggregate structure tend to occur as the particles age and obtain moisture [e.g., ?], contributing to a reduction in MAC with atmospheric lifetime. But particle coating from condensation of weakly-absorbing material increases MAC (specific to the original BC mass) [e.g., ?]. ? suggest that the net effect of these competing processes increases MAC by a factor of ~ 1.5 with aging. With this information, we treat aged, hydrophilic BC as sulfate-coated. We apply Mie theory, using the same core properties as hydrophobic BC and a sulfate coating with outer radius 1.67 times that of the uncoated BC, yielding an absorption enhancement of 1.5 at $\lambda = 550 \text{ nm}$. Optical properties are applied consistently to these two aerosols in the atmosphere and snow. Uncertainty remains about BC/ice mixing states. We assume external mixtures of coated and uncoated BC, but BC coating by sulfate mimics that by ice, since both coatings are weakly absorbing. Furthermore, for small core diameters, increasing coating thickness only slightly increases the absorption amplification [?].

We apply OPAC optical properties [?] for water-soluble aerosol to atmospheric OC [??], but do not treat OC in the snowpack. A short GCM sensitivity study with active OC in snowpack showed global forcing $200\times$ smaller than BC/snow forcing using these optical properties. However, several recent studies [e.g., ????] showing carbon aerosol absorption features with Angstrom coefficients greater than 1, and other chemical analyses, lead ? to state “there is clearly a substantial fraction of organic matter in fine atmospheric aerosol, which is light-absorbing, but has properties and origins very much different from soot and is definitely not black.” This “brown carbon” is characterized with Angstrom coefficients from 2 – 6, and is emitted in greater quantity from biomass burning and low-temperature combustion. Future research constraining OC emissions, atmospheric processes, optical properties, and snow concentrations may show that OC is a non-negligible absorber in snowpack.

2.3. Snow Aging

As discussed later, the change in absorbed energy caused by BC depends strongly on snow r_e , implying that forcing is sensitive

to snow aging. We apply an empirical representation of the microphysical model developed in ?, which predicts the evolution of snow specific surface area with dependence on snow temperature, temperature gradient, and density. In our model, large temperature gradients can reduce pure snow, spectrally-averaged albedo by up to 0.12 within 14 days, but the influence of temperature gradient is marginalized by cold temperature and high snow density. The predictive aging equation used here is the time derivative of Equation 16 in ?:

$$\frac{d\hat{S}}{dt} = \frac{1}{\kappa} \hat{S}_0 \tau^{1/\kappa} (t + \tau)^{-1/\kappa - 1} \quad (2)$$

where \hat{S} is the snow specific surface area, \hat{S}_0 is the fresh snow specific surface area (assumed to be $60 \text{ m}^2 \text{ kg}^{-1}$), t is the time since snowfall (where snowfall of 10 mm liquid water equivalent completely resets snow age and SSA), and κ and τ are best-fit parameters to predictions from the microphysical model, retrieved from a lookup table depending on local snow temperature, temperature gradient, and density. Finally, since effective radius is a surface area-weighted radius, $r_e = 3/(\hat{S} \rho_i)$, where ρ_i is bulk ice density. Model temperature gradient is taken as the mean gradient at the center of each snow layer in CLM, and for snow on sea-ice as the temperature difference between surface air and the mean of sea-ice and snow temperatures, divided by the snow layer thickness. With a single snow layer, CSIM cannot resolve the strong temperature gradient that often exists in near-surface snow, and hence likely underestimates aging. We also add a wet snow grain growth function, based on laboratory measurements, that is parameterized as a function of liquid water content [?]. Grain growth from liquid water transfer is still very poorly understood, and this function likely applies only to a limited set of snow condition. To enable wet snow aging in CSIM, we added diagnostic prediction of liquid water content based on net energy balance of snow at the freezing temperature. Our aging parameterization does not treat effects of wind, melt-freeze cycles, and sintering. Large uncertainties remain about snow aging because of the complexity of governing processes and because few quality observational datasets exist to help understand those processes. Hence, we consider half and double the rate of r_e evolution predicted by SNICAR for our low and high estimates, respectively.

2.4. Meltwater Scavenging and Aerosol Removal

Very few studies have examined meltwater scavenging of impurities in snow. CLM accounts for meltwater drainage by adding excess water to the layer beneath when liquid content exceeds the layer's holding capacity, defined by snow porosity and irreducible water saturation. We assume BC inclusion in meltwater proportional to its mass mixing ratio multiplied by a scavenging factor. Thus, the BC mass rate of change in each layer i is:

$$\frac{dm_i}{dt} = k(q_{i+1} c_{i+1} - q_i c_i) + D \quad (3)$$

where m is the absolute mass of BC in each layer, k is the scavenging ratio, q_i is the mass flux of water out of layer i , c_i is the mass mixing ratio of BC in layer i (BC mass divided by liquid+solid H_2O mass), and D is the sum of wet and dry atmospheric deposition, added only to the surface layer. This equation has similar form to Equation 2 of ? but is generalized for multiple snow layers and treats removal as a function of meltwater scavenging rather than with an empirical fall speed. After deposition, BC is instantly mixed uniformly in the model surface layer, which never exceeds 2 cm thickness.

? applied BC to the surface of melting snow and observed that 99% of hydrophilic BC, and 50% of hydrophobic BC were removed from the top 50 cm of snow after 10 days. Applying a simple e-folding model with total meltwater production observed during this period, and initial and final BC mass observed in the top 2 cm, we estimate hydrophilic and hydrophobic scavenging ratios of $k_{\text{phi}} = 0.037$ and $k_{\text{pho}} = 0.031$. This estimate of k_{phi}

is likely too small, because nearly all of the hydrophilic BC retained in the top 50 cm was in the top 2 cm and ? note that particles larger than $\sim 5 \mu\text{m}$ are relatively immobile during melt. Therefore, retention of hydrophilic particles near the snow surface is likely because of size rather than particle affinity for water. This is consistent with observations of mineral dust particles (typically larger than BC by 2-3 orders of magnitude) remaining near the surface during snowmelt [Tom Painter, personal communication, 2006]. ? offers unique observations of aerosol transport with snow meltwater, but the spatial and temporal resolution of observations are too coarse, and uncertainty about the role of particle size too large, to estimate scavenging ratios with much confidence. Here, we assume $k_{\text{pho}} = 0.03$, derived from observations in the top 2 cm, and apply the $k_{\text{pho}}/k_{\text{phi}}$ ratio obtained from analysis of observations in the top 50 cm of snow to obtain $k_{\text{phi}} = 0.20$. For high and low estimates, we assume an order of magnitude uncertainty (Table 1).

In the absence of melt, fresh snowfall in CLM continuously divides the model surface snow layer and prevents excessive BC accumulation. In CSIM, BC accumulates excessively in snow on perennial sea-ice because of the single layer representation and because snow remains perennially on the sea-ice (an issue discussed later). Consequently, we impose empirical BC removal with an e-folding time of 1.44 years, resulting in steady-state interannual concentrations. Future versions of this sea-ice model will have multiple snow layers.

2.5. Snow Cover Fraction

Snow cover fraction (SCF) controls the area over which BC/snow forcing operates. SCF is generally parameterized as a simple function of snow depth, but also depends on orographic variability, vegetation cover, and melt/accumulation phase [Z. Liang-Yang, personal communication, 2006]. We found seven widely-varying SCF representations in the literature and choose the following, based solely on their relative scales, for low, central, and high SCF relationships to snow depth:

- Low: $\text{SCF} = d/(10z + d)$. [?] (CLM)
- Central: $\text{SCF} = \min[1.0, \log(100d + 1)/3.33]$ [?]
- High: $\text{SCF} = \tanh[d/(2.5z)]$ [?]

Here, d is snow depth (m) and z is surface roughness length (fixed at 0.01 m for all soil types and glacier surfaces in CLM).

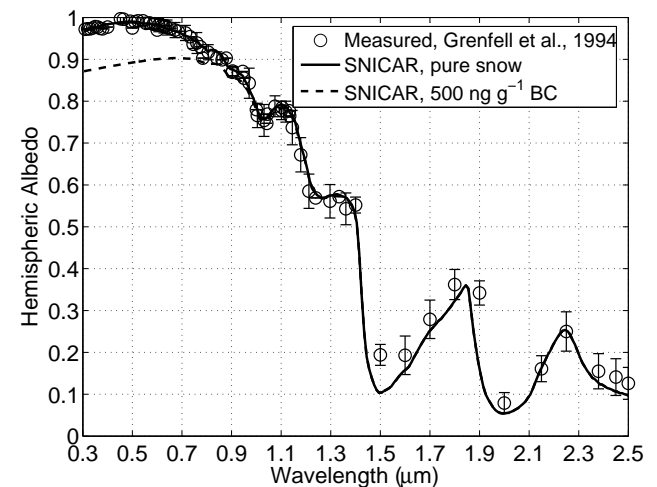


Figure 2. Measured diffuse incident radiation snow albedo at the South Pole from ? and modeled albedo from SNICAR assuming a 0.25 mm thick surface layer composed of $45 \mu\text{m}$ r_e snow and a deep underlying layer of $100 \mu\text{m}$ r_e snow. The thin surface layer controls reflectance in the highly-absorptive NIR portion of the spectrum. Also shown is modeled snow reflectance with 500 ng g^{-1} of hydrophilic (coated) BC.

Snow depth of 10 cm predicts SCF of 0.47, 0.69, and 0.99 for these three representations, respectively. τ is the current implementation in CLM. τ relates snow depth, as measured by stations in the U.S. and Canada, to SCF observed by satellite. Their derived relationship is valid for snow depths less than 30 cm over prairies and lightly-forested regions. τ propose SCF from analysis of six years of station data from six sites in the Former Soviet Union. Improving SCF representation to account for variables other than snow depth is beyond the scope of this study.

Lacking a radiative transfer approximation for BC inclusion in sea-ice, we assume snow forcing acts homogeneously over snow-covered and snow-free ice. This crude assumption probably underestimates forcing, because surface sea-ice is very coarse-grained [e.g. τ], and forcing increasing with increasing r_e .

3. Results and Discussion

In this section we first compare spectral albedo from SNICAR with observations and examine sensitivity of snow albedo and sub-

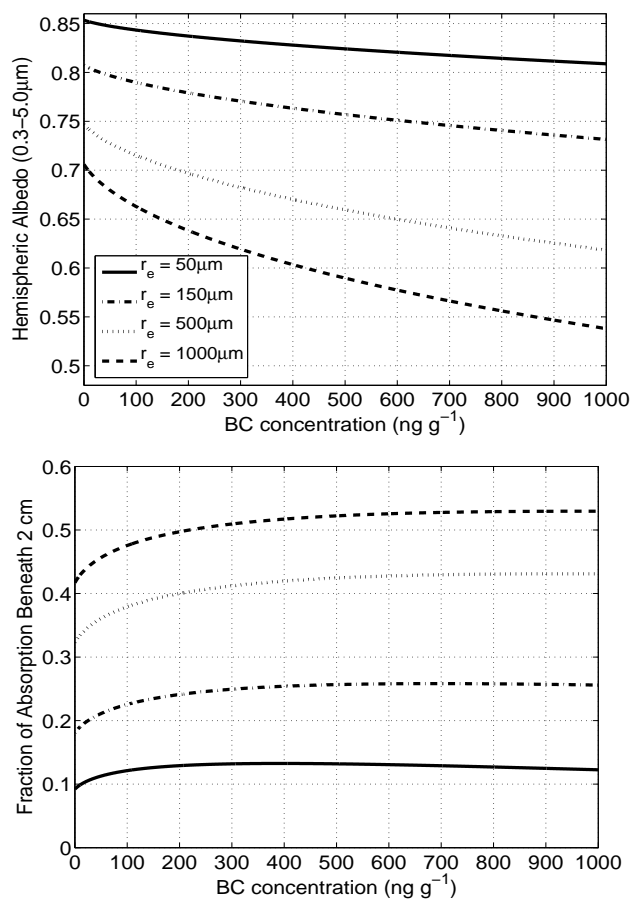


Figure 3. (top) Spectrally-averaged snow albedo as a function of BC mass concentration for various snow effective radii (r_e). Note that BC perturbs albedo more in larger-grained snow. (bottom) Fraction of total snowpack absorption occurring more than 2 cm beneath the surface as a function of BC concentrations for the same r_e as the top panel. Absorption occurs deeper in the snow with homogeneously-mixed BC because more of the total absorption is from visible radiation, which tends to absorb deeper than NIR, even with large BC concentrations. In both experiments, the snowpack is optically semi-infinite and homogeneous. Incident flux is direct-beam from 60° zenith angle. For comparison of these BC concentrations with global observations and model predictions see Table 2 and Figures 4 and 5.

surface radiative heating to varying BC concentrations and snow effective radii. Next, we analyze GCM experiments with BC in snow, first comparing predicted BC concentrations in snow with observations, then assessing global forcing, and finally examining climate feedbacks.

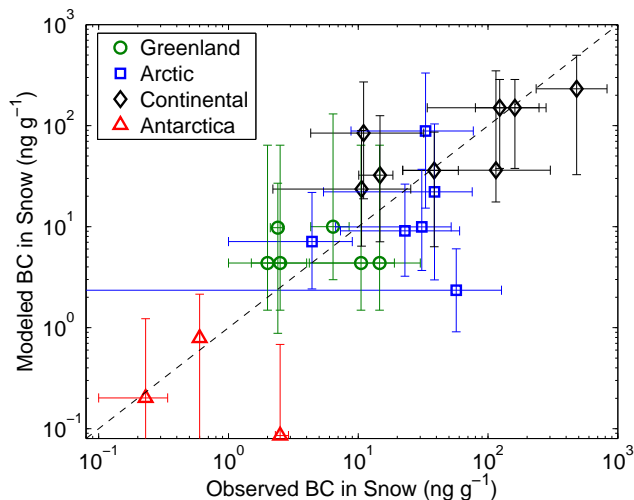


Figure 4. Model vs. observed BC concentrations in near-surface snow for data from Table 2, grouped by region (precipitation measurements excluded). Model data are from the top 2 cm of snowpack. The center model point on this plot is the mean of 1998 and 2001 central experiments. The upper extent of the model error bar represents the maximum of 1998 and 2001 high experiments, whereas the lower extent is the minimum of both low experiments. The correlation coefficient of the log of these data is 0.78.

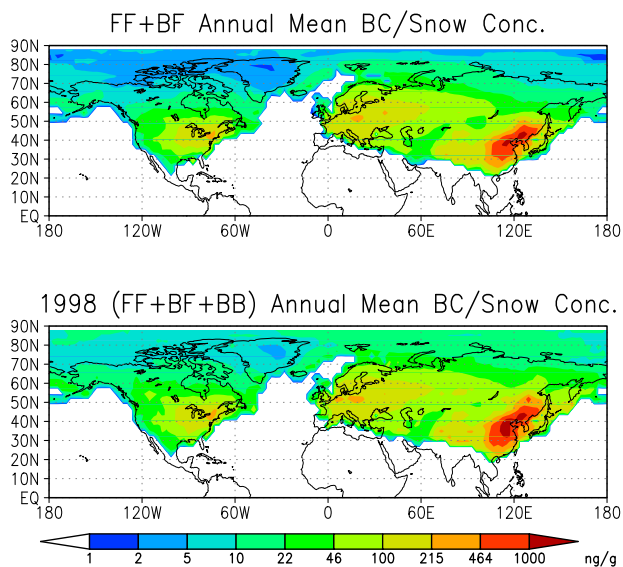


Figure 5. Annual mean predicted BC concentrations in snow (ng BC per g of ice) using central estimate (top) fossil fuel and biofuel sources only, and (bottom) fossil fuel, biofuel, and 1998 biomass burning emission sources.

Table 2. Comparison of Modeled and Measured BC in Snow, Sea-Ice, and Precipitation

Site	Reference	Measurement Period	Measured BC [ng g ⁻¹] ^a	1998 Model BC central (low–high)	2001 Model BC central (low–high)
Summit, Greenland (72.6°N, 38.5°W)	?	1994-1996	14.6(4.2 – 30.1)	5.2(1.7 – 64.1)	3.5(1.5 – 34.5)
	?	1991-1995	2.0 – 19.0 ^b		
	?	1989-1990	2.0(1.5 – 2.7)		
	?	1988-1989	1.0 – 4.0 ^b		
	?	~ 1985	2.4(2.1 – 2.6)	13.3(1.2 – 26.9)	6.2(0.9 – 19.6)
Dye 3, Greenland (65.2°N, 43.8°W)	?	May 1983	6.4(4.3 – 8.5)	11.8(3.6 – 131)	8.2(3.0 – 29.1)
Alert, N. Canada (83.5°N, 62.5°W)	?	Nov.-Dec. 1983	56.9(0 – 127)	2.2(0.9 – 5.9)	2.5(1.0 – 6.0)
Greenland Sea (79.8°N, 4.2°W)	?	Jul. 1983	38.7(5.4 – 75.5)	23.9(3.0 – 104)	20.4(3.5 – 93.9)
Spitzbergen (79°N, 12°E)	?	May 1983	30.9(6.7 – 52)	12.7(3.7 – 37.0)	7.2(4.6 – 34.4)
Barrow (71.3°N, 156.6°W)	?	Apr. 1983, Mar. 1984	22.9(7.3 – 60.4)	9.7(4.1 – 26.4)	8.4(3.2 – 25.4)
Abisko (68.3°N, 18.5°E)	?	Mar.-Apr. 1984	33.0(8.8 – 77)	80.7(15.3 – 332)	96.4(19.4 – 279)
Hurricane Hill (48.0°N, 123.5°W)	?	Mar. 1984	14.7(10.1 – 18.5)	29.5(7.1 – 101)	35.2(7.1 – 125)
Arctic Ocean (76°N, 165°E)	?	Mar.-Apr. 1998	4.4(1 – 9)	8.4(4.2 – 21.8)	5.8(2.4 – 16.7)
Cascades, Wash (~47°N, 121°W)	?	Mar. 1980	22 – 59	36.8(6.3 – 86.3)	35.1(6.7 – 85.9)
Halifax, Nova Scotia (45°N, 64°W)	?	Nov. 1995-Mar. '96	11(4.3 – 32)	84.0(22.0 – 244)	84.9(18.9 – 270)
French Alps (45.4°N, 5.3°E)	?	winters 1989-'91	161(80 – 280)	165(50.5 – 226)	136(37.7 – 287)
	?	winters ~1992-'97	123(34 – 247)		
	?	Apr. 1992	482(235 – 826)	394(92.2–) ^c	69.4(32.7 – 498) ^c
	?	Dec. 1992	115(22 – 302)	29.0(37.4 – 349)	43.5(17.6 – 51.5)
	?	1982-'85	10.6(2.2 – 25.4)	31.6(8.4 – 89.6)	15.5(6.4 – 73.0)
West Texas/New Mexico (32°N, 106°W)	?	1982-'85	10.6(2.2 – 25.4)	31.6(8.4 – 89.6)	15.5(6.4 – 73.0)
Vostok (78.5°S, 106.9°E)	?	Dec. 1990-Feb. '91	0.6	1.08(0.07 – 2.1)	0.50(0.07 – 1.8)
Siple Dome, Ant. (81.7°S, 148.8°W)	?	1982-'85(?)	2.5(2.3 – 2.9)	0.08(0.04 – 0.68)	0.09(0.04 – 0.51)
South Pole (90°S)	?	Jan.-Feb. 1986	0.23(0.10 – 0.34)	0.20(0.07 – 1.23)	0.21(0.06 – 1.2)
BC in Precipitation					
Rural Michigan (45.5°N, 84.7°W)	^d	Dec.-Apr 1984-'85	72(28 – 210)	50(22 – 108)	46(21 – 98)
Urban Michigan (42.5°N, 83°W)	^d	Jan.-Apr 1984-'85	160(17 – 5700)	57(26 – 132)	53(23 – 113)
Lithuania (55.5°N, 21°E)	^e	Dec. 1986-Jun. '90	100(8 – 530)	61(22 – 177)	56(20 – 179)

^a When mean values are not reported in the original literature, we report means of all published values from each location

^b as reported in ?

^c model results from March used in place of April; no March snow in 1998 high experiment

^d snow precipitation

^e snow+rain precipitation

3.1. BC Influence on Snow Albedo and Radiative Heating

We first apply offline, single-column, 470-band SNICAR to demonstrate model fidelity in reproducing observed snow reflectance. Figure 2 shows measured snow albedo for diffuse incident radiation at the South Pole [Figure 4 of ?, data provided by Steve Warren] and modeled reflectance using SNICAR with a thin (0.25 mm) surface layer composed of 45 μm r_e snow and a thick underlying layer composed of 100 μm r_e (snow density = 350 kg m⁻³). ? found that a similar 2-layer model (with surface $r_e = 30 \mu\text{m}$) also matched observed reflectance in both the visible and absorptive NIR. Because they did not measure snow grain size at the very high vertical resolution needed for model testing with fully-known snow conditions, ? point out that many arbitrary layer thickness and r_e model combinations can produce a good fit. Also shown in this figure is modeled albedo of the same snowpack, but with 500 ng g⁻¹ of hydrophilic (coated) BC. The BC strongly reduces visible reflectance, but has negligible influence at wavelengths beyond 1 μm .

Next, we identify how varying concentrations of BC affect spectrally-averaged (0.3 – 5.0 μm) hemispheric snow albedo and subsurface heating with different r_e . We assume an optically thick, homogeneous snowpack with direct-beam incident flux at a solar zenith angle of 60°. ? report that, using the model of ?, a uniform distribution of 15 ng g⁻¹ BC reduces albedo by 1% at 500 nm with an effective grain radius of 100 μm . In our model, hydrophobic and hydrophilic BC reduce 500 nm albedo in snow with $r_e = 100 \mu\text{m}$ by 0.0079 and 0.0108, respectively. The experiments discussed below apply hydrophobic BC optical properties.

Figure 3 (top) shows spectrally-averaged snow albedo for BC concentrations ranging from 0 – 1000 ng g⁻¹, and four different r_e . Qualitatively, these curves agree well with Figures 1 and 2 of ?. As originally noted by ?, the presence of absorbing impurities reduces albedo more in snow with larger r_e . Albedo reduction for 1000 ng g⁻¹ BC is 0.17 and 0.045 for snow with $r_e = 1000$ and 50 μm , respectively. Both the absolute perturbation from BC and disparity in perturbation between grain sizes grow as zenith angle decreases.

The grain size effect is somewhat counterintuitive, as one naturally expects brighter media to be more susceptible to darkening

by impurities. But visible radiation penetrates deeper in snow with larger r_e because it has a smaller extinction coefficient and, less importantly, scatters more strongly in the forward direction. The snow depth where mean radiative intensity diminishes to 1/ e of its surface value is 17 cm for $r_e = 50 \mu\text{m}$ and 78 cm for $r_e = 1000 \mu\text{m}$ ($\lambda = 550 \text{ nm}$, snow density = 150 kg m⁻³, zenith angle = 60°). By traveling through a greater optical depth of impurities, photons thus have a greater probability of absorption by (homogeneously-interspersed) impurities in snow with larger r_e . Sensitivity to grain size highlights the importance of snow aging treatment and realistic r_e , which can vary significantly on small spatial scales [?].

Nearly all albedo reduction from BC is due to increased absorption in the visible spectrum. NIR albedo decreases by only 0.02 – 0.06 with 1000 ng g⁻¹ BC, whereas visible albedo is reduced by 0.07 – 0.28 (not shown). This produces another surprising result: with homogeneously mixed BC, the fraction of total absorption occurring more than 2 cm beneath the snow surface *increases* with increasing BC amount, up to a limit. Figure 3 (bottom) shows this fraction increasing by up to 0.11 with $r_e = 1000 \mu\text{m}$. While BC shifts the visible absorption to nearer the surface, a much greater portion of total absorption is in the visible spectrum. Even with large BC concentrations, visible absorption tends to occur deeper than NIR absorption. Most NIR absorption occurs in the top 1 mm of snow [?]. With sufficiently high BC concentrations however, absorption shifts to higher in the snowpack, as can be seen by the slight downward trend in sub-2 cm absorption for $r_e = 50 \mu\text{m}$ and BC concentrations greater than 400 ng g⁻¹. The BC concentration of maximum sub-2 cm absorption depends on r_e because of the visible depth-penetration dependence on r_e . If aerosol is more concentrated at the snow surface, however, due to dry deposition or accumulation of impurities near the snow surface during melt, total absorption shifts towards the surface. By influencing sub-surface melt [?], changes to the vertical distribution of heating can have important influence on snow climatology [?].

3.2. GCM Experiments

We conducted six GCM experiments with BC in snow, using configurations presented in Table 1, designated from here on as

YYYY low, central, or high experiment, where YYYY is 1998 or 2001. To assess climate response and efficacy, we also completed paired control simulations for the central and high experiments, (YYYY central and high control), identical to the experiments except without BC in snow. Forcing in the low experiments was insufficient to perturb climate. To help constrain efficacy, we also conducted experiment and control simulations with $10\times$ 1998 BC and OC emission inventories (1998 $10\times$ experiment and control), with otherwise central model configurations (Table 1). Finally, to help discern the relative forcing contributions from FF, BF, and BB sources, we conducted experiments emitting only FF+BF and FF central estimate sources (FF+BF and FF experiments). All runs apply annually-repeating emissions.

The wide range of climate perturbation in these experiments required different spinup periods for equilibrium. In the discussion that follows, we report results from the final 15 years of 16-year simulations (1998 and 2001 low, FF+BF, and FF experiment), 25-year simulations (1998 and 2001 central experiments and controls), and 35-year simulations (1998 and 2001 high experiments and controls). For the 1998 $10\times$ experiment and control, we analyze the final 20 years of 50-year simulations. The 95% confidence interval of linear trend in global mean 2-meter air temperature (T_{2m}) of these 15- and 20-year timeseries included zero for all experiments and controls except 2001 central and high experiments, which both had trends of $+0.01^\circ\text{C yr}^{-1}$. Because the corresponding controls had no trend, it is possible we underestimated the climate response for these scenarios. Global mean top-of-model (TOM, about 3 mb pressure) radiative energy flux, averaged over the analysis periods, was within 1 W m^{-2} of equilibrium for all model runs.

3.3. Measured and Modeled BC Concentrations in Snow

Table 2 summarizes measurements of present-day BC in snowpack from all studies known to the authors. When mean values are not reported in the original literature, we report means of all published measurements from each location. Measurement techniques and uncertainties vary considerably between studies and are discussed to varying degrees in each reference. Most studies utilize optical or thermal/optical techniques, although ? applies an acid-base/thermal method. Table 2 also shows CAM/SNICAR predictions of BC concentrations in the surface snow layer. Data in the lower portion of the table show BC concentrations in precipitation, with model estimates derived from wet deposition and precipitation rates. When the measurements correspond to a particular time of year, we report model predictions from the same months. Otherwise, model results are annual mean estimates. Central estimates for 1998 and 2001 are reported with low–high range in parentheses. A log-log whisker plot of these data is shown in Figure 4. The center model point on this plot is the mean of 1998 and 2001 central experiments, and vertical error bar represents the greatest minimum–maximum range from both 1998 and 2001 low and high experiments. Global distributions of model annual mean BC concentrations in surface snow, averaged only when snow is present, are shown in Figure 5 for FF+BF and 1998 (FF+BF+BB) central estimates, plotted on a log-scale.

Figure 4 shows that central estimate BC/snow predictions capture the nearly 4 orders of magnitude range in observations with no apparent systematic bias. The correlation coefficient of the log of central model estimates and mean observations is 0.78. Furthermore, in nearly all cases there is some overlap between the range of measurements and low–high model predictions.

Central model predictions are within the range of observations on Greenland and Antarctica, indicating reasonable model long-range BC transport. An exception is Siple Dome, where ? report measurements an order of magnitude greater than more recent Antarctic observations [??]. Measurements in Table 2 are not time-resolved, except for ?, who reports elemental carbon (EC, often considered synonymous with BC) concentrations with quarter-annual resolution, varying from $4 - 30\text{ ng g}^{-1}$ over the course of

two years. EC concentration spike in the fall of 1994, although ^{14}C analysis shows a predominantly fossil fuel-derived source. At Summit, monthly-mean BC concentrations vary from $2 - 10$ and $7 - 330\text{ ng g}^{-1}$ in our 1998 central and high estimate experiments, respectively, peaking in August and July.

None of the measurements overlap our two years of emission scenarios. Because of interannual variability in biomass burning and trends in regional fossil fuel use, validity of this model-measurement comparison is therefore reduced. For example, our predictions are lower than four arctic measurements [?] made in the early 1980's, when BC emissions from the Former Soviet Union were much greater than today [?].

Conversely, predictions exceed measurements at Abisko (Sweden), Hurricane Hill (Washington) [?], and Halifax [?]. While Hurricane Hill may be representative of long-range transport because of prevailing westerlies, it is in the same model gridcell as Seattle and has a large local source. Measurements east of Seattle by ? show double the concentrations from Hurricane Hill, in accord with central model predictions. Halifax has a smaller, but still significant local source. ? specifically measure urban areas, however, so our model may have a high-bias in this region. Low predictions are in range of measurements at Halifax and Abisko. In the French Alps near Grenoble, central model estimates agree well with ? and ?, but are lower than ?. Central estimates of BC concentrations in precipitation are within range of measurements in rural Michigan [?] and Lithuania [?], although are lower than measurements made near Detroit [?].

The largest predicted BC concentrations in snow are in north-east China (Figure 5), near strong industrial sources. There, concentrations in excess of 1000 ng g^{-1} can lower snow albedo by more than 0.13. Annual mean concentrations in the eastern U.S. and Europe exceed 100 ng g^{-1} , enough to lower snow albedo by > 0.03 , depending on r_e . While fossil fuel-derived BC is the dominant source of mid-latitude BC in snow, the effect of strong 1998 wildfires can be seen across the Arctic and Greenland (Figure 5). Annual mean BC concentrations in snow averaged over Greenland are 44% greater in 1998 than 2001. Comparing with the FF+BF simulation, we estimate that 43% and 24% of the annual mean BC in arctic snow ($66.5 - 90^\circ\text{N}$) is from biomass sources in 1998 and 2001, respectively. During summer (June, July, August) these BB source fractions rise to 60% and 36%.

Summer atmospheric conditions favor enhanced wet and dry arctic BC deposition rates [?], implying greater summer BC concentrations in snow regardless of temporal variability in emissions. ? predict that south Asia is the largest source of tropospheric arctic BC, but ? contests this and predicts that biomass sources dominate summer arctic BC using a mean 1980's burning inventory [?]. ? also suggests that Siberian fires, and northern Eurasia sources in general, can reach the Arctic more easily than emissions from other regions of similar latitude. Future studies should use re-analysis winds to study the impact of individual fire events.

3.4. Global Mean Forcing and Response

Table 3 lists for all experiments (from left to right) the global mean instantaneous surface forcing from BC in snow ($F_{s,\text{snow}}$), the fraction of $F_{s,\text{snow}}$ acting over land (where the remaining fraction operates over sea-ice), $F_{s,\text{snow}}$ averaged temporally and spatially only over snow-covered land surface, $F_{s,\text{snow}}$ averaged only over sea-ice, the change in global annual mean T_{2m} (ΔT_{2m}) relative to control simulations without BC in snow, forcing “efficacy,” and finally top-of-model (TOM) forcings from atmospheric BC+OC ($F_{t,\text{atm}}$). Efficacy is defined as [?]:

$$E = \frac{\Delta T_s / F_a}{\Delta T_s(\text{CO}_2) / F_a(\text{CO}_2)} \quad (4)$$

where F_a is the forcing at the tropopause after stratospheric adjustment [e.g., ?] and ΔT_s is the change in global mean surface air temperature. The denominator is the response-to-forcing ratio from CO_2 . ? use forcing and temperature response from $1.5\times$

Table 3. Summary of Model Experiment Results

Model Scenario	$F_{s,snow}^a$ [W m ⁻²]	Land frac. ^b of $F_{s,snow}$	$F_{s,snow} LAND^c$ [W m ⁻²]	$F_{s,snow} ICE^d$ [W m ⁻²]	ΔT_{2m}^e [°C]	Efficacy ^f	$F_{t,atm}^g$ [W m ⁻²]
1998 low	+0.007 ± 8%	0.73	+0.08	+0.04	–	–	+0.07 ± 14%
1998 central	+0.054 ± 7%	0.82	+0.60	+0.23	+0.15 ± 0.03	4.52 ^{+0.98} _{-0.97}	+0.37 ± 2%
1998 high	+0.131 ± 6%	0.83	+1.56	+0.79	+0.23 ± 0.02	2.83 ^{+0.35} _{-0.34}	+1.31 ± 1%
2001 low	+0.007 ± 9%	0.74	+0.07	+0.04	–	–	+0.05 ± 11%
2001 central	+0.049 ± 7%	0.83	+0.55	+0.20	+0.10 ± 0.03	3.29 ^{+1.12} _{-1.11}	+0.28 ± 2%
2001 high	+0.122 ± 6%	0.83	+1.42	+0.75	+0.16 ± 0.03	2.11 ^{+0.37} _{-0.37}	+1.09 ± 1%
FF+BF	+0.043 ± 5%	0.85	+0.48	+0.15	–	–	+0.19 ± 5%
FF	+0.033 ± 6%	0.85	+0.26	+0.12	–	–	+0.10 ± 4%
1998 10×	+0.277 ± 3%	0.77	+2.90	+1.11	+0.54 ± 0.02	3.11 ^{+0.15} _{-0.14}	+4.96 ± 1%

^a Global annual mean of BC/snow instantaneous surface forcing

^b Fraction of $F_{s,snow}$ acting over land

^c $F_{s,snow}$ averaged spatially and temporally only over land snowpack

^d $F_{s,snow}$ averaged spatially and temporally only over snow on sea-ice

^e Equilibrium change in global annual mean T_{2m} relative to control simulations without BC in snow

^f (See Equation 4)

^g Global annual mean top-of-model (TOM) forcing from atmospheric BC+OC

pre-industrial CO₂ levels. We apply CAM3 slab ocean model results from ?, who report $F_a(\text{CO}_2) = 3.58 \text{ W m}^{-2}$ and equilibrium $\Delta T_s(\text{CO}_2) = 2.47^\circ\text{C}$ from a doubling of CO₂ (355 – 710 ppm). In deriving F_a from $F_{s,snow}$, we assume that instantaneous forcing at the tropopause (F_i) is $0.91 F_{s,snow}$, and that F_a is equal to F_i (e.g., there is negligible immediate stratospheric radiative adjustment to the surface forcing). The first assumption is derived from numerous offline experiments with SWNB [?]. We examined the change in net solar energy at 132 mb relative to that at the surface (F_i/F_s) for slight reductions in visible surface albedo of a typical snow surface (initial visible and NIR albedos of 0.97 and 0.60). With zenith angle varying from 20 – 70°, cloud extinction optical depth τ_{cld} varying from 0 – 50, and visible albedo reduction varying from 0 – 0.10, the ratio F_i/F_s varies only from 0.94 – 0.96. While F_s is substantially reduced under cloudy skies, F_i/F_s remains large and constant. However, absorbing aerosol significantly reduces F_i/F_s , particularly when it resides beneath a cloud, as multiple scattering between snow and cloud enhances absorption by the aerosol. Absorption optical depth $\tau_a = 0.05$ ($\lambda = 550 \text{ nm}$) can reduce F_i/F_s to 0.44. But assuming global mean $\tau_a = 0.0096$ inferred from AERONET scaling of aerosol climatologies [??], $\tau_{\text{cld}} = 5$, and zenith angle of 60°, we estimate $F_i/F_s = 0.91$, which we apply to derive efficacy. The ranges reported in Table 3 represent standard deviation in the annual-mean timeseries. The reported range of ΔT_{2m} assumes unpaired pools (of global mean temperature from each year of equilibrium simulation) with equal variance. Efficacy standard error combines, in quadrature, standard deviations of $F_{s,snow}$ and ΔT_{2m} . Support for our second assumption (that F_a equals F_i) comes from ?, who report F_a for BC/snow forcing within 2% of F_i .

Table 3 shows that global BC/snow forcing is small relative to forcing from atmospheric BC+OC (columns 'a' and 'g' in Table 3). When $F_{s,snow}$ is averaged spatially and temporally only over snow, however, central estimates suggest that 0.55 – 0.60 additional W m^{-2} are absorbed by snowpack on land and 0.20 – 0.23 W m^{-2} by sea-ice because of the immediate presence of BC in snowpack. Our central estimates of $F_{s,snow} = +0.054$ and $+0.049 \text{ W m}^{-2}$ predict ~ 10% greater forcing in 1998 than 2001. Comparison with the FF+BF run suggests that about 20% of the total forcing can be attributed to biomass burning in 1998 and 12% in 2001. Estimates from ? of $F_a = +0.16 \text{ W m}^{-2}$ were downgraded to $+0.05 \text{ W m}^{-2}$ [?, corrected result published in Appendix A.5 of ?]. The latter estimate is derived from spatially-varying BC deposition, but without a detailed radiative transfer solution for snow with BC.

An estimate of F_a from FF+BF BC in snow and ice from ? is $+0.06 \text{ W m}^{-2}$ [Mark Jacobson, personal communication, 2006], greater than our estimate of $+0.039 \text{ W m}^{-2}$ ($0.91 \times 0.043 \text{ W m}^{-2}$). ? treats BC in snow with a radiative transfer approximation, but prescribes spatially and temporally uniform snow grain size and an empirical fall-speed for BC removal from snowpack. Atmospheric aerosol and cloud physical processes are highly

sophisticated in ?, however. Size-resolved BC and hydrometeors (including graupel) interact in clouds and precipitation through nucleation and coagulation, and both first and second aerosol/cloud indirect effects are treated. These processes enable prediction of more realistic size distribution and mixing state of BC deposited on snow. Because BC ages rapidly in our model relative to the transport time from source to remote snow surface, 87% of the BC deposited on snow is via wet deposition (providing a minimum estimate of the hydrophilic BC fraction in snow). This is less than the 98% BC wet deposition fraction on snow reported by ?, but likely greater than ?, who report that dry deposition is responsible for the majority of BC landing on Greenland. Model differences could be due to several reasons, including more explicit treatment of size-resolved in-cloud scavenging processes by ?, different dry deposition velocities, and different spatial pattern of emissions relative to model snow cover.

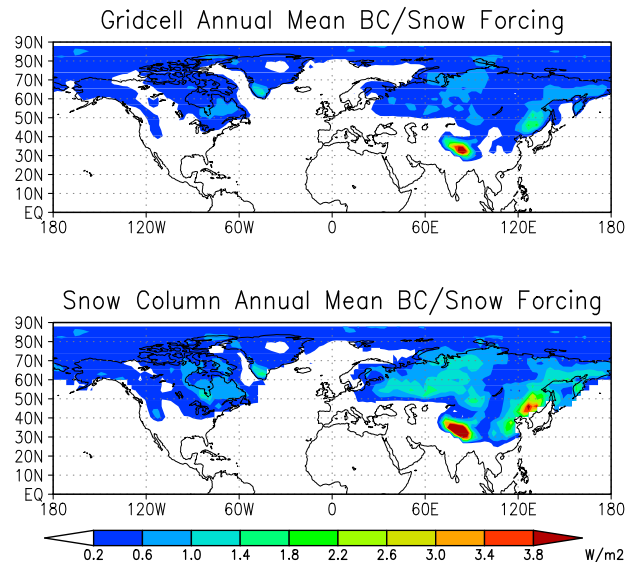


Figure 6. Central estimates of 1998 surface forcing (W m^{-2}) from BC in snow; (top) annual mean gridcell forcing, representing the true climate forcing; (bottom) forcing averaged spatially and temporally over only snow-covered surface, representing the mean increase in energy absorption by snowpack.

While $F_{s,snow}$ is small globally, its efficacy is very large. Mean efficacy from the 5 experiment/control pairs in Table 3 is 3.17(2.1–4.5). Because the temperature signal/noise ratio is small for realistic (e.g., central estimate) BC/snow forcing, the 1998 10 \times experiment and control provide a more constrained efficacy estimate. (More years of analysis also improve statistical constraint of the temperature response). Tight agreement between 1998 10 \times efficacy and the mean of the other experiments is also encouraging. We caution, however, that efficacy does not necessarily scale linearly with forcing magnitude for a given agent [Figure 25 of ?]. Global mean T_{2m} cooled several degrees before achieving steady-state in both 1998 10 \times experiment and control runs because of extreme atmospheric aerosol optical depth, in spite of a positive TOM aerosol forcing.

? report similarly large BC/snow efficacy of 2.7 (corrected result in Appendix A.5 of ?), the largest efficacy of all forcings studied. Conversely, mean efficacy of atmospheric BC (~ 0.69) is less than CO_2 [?]. Possible reasons for even greater BC/snow efficacy in our study include 1) greater albedo change sensitivity to temperature change in the IPCC AR4 NCAR model relative to the GISS model [?], 2) representation in our model of impurity accumulation near the surface during spring melt, which enhances the forcing precisely when it can have the largest impact on snowmelt and thus snow-albedo feedback, and 3) representation in our model of dynamic snow grain growth, which is enhanced by excess snowpack heating from BC. Better constraint on efficacy will require larger ensembles of GCM simulations with varying initial conditions, and is beyond the scope of this study.

Forcing from atmospheric BC+OC ($F_{t,atm}$) is about 5–6 \times greater than BC in snow (Table 3). However, if forcings are scaled by their respective efficacies, as ? suggest, the resulting atmospheric BC+OC and BC/snow “effective” forcings are of similar magnitude. Much of the forcing from atmospheric BC is offset by OC, which is emitted simultaneously as BC in greater proportion, and which strongly scatters solar radiation. The net effect of atmospheric BC+OC forcing depends on aerosol optical properties, relative aerosol quantities, and reflectance of the underlying surface [e.g., ?]. The OC/BC emission ratio is smaller in FF combustion than BB [e.g., ?]. Hence, net radiative forcing from FF BC+OC is positive [e.g., ?], whereas the sign of net forcing from BB BC+OC could be positive [e.g. ?] or negative [e.g., ?], depending especially on whether aerosol is lofted above clouds, where it is much more likely to have positive forcing. However, many other scattering aerosols are emitted in significant quantity from biomass burning, leading ? to suggest a global net surface cooling effect from all biomass burning aerosols. In our study, biomass burning contributes a much greater portion to $F_{t,atm}$ (49% and 32% in 1998 and 2001 central estimates, respectively) than to $F_{s,snow}$ (Table 3). Atmospheric aerosol forcing is not the focus of this study though, so we refrain from a detailed analysis.

3.5. Spatial/Temporal Climate Response Patterns

The primary reason why BC/snow forcing is so efficacious is its ability to trigger snow-albedo feedback. Here, we look at spatial and temporal distributions of forcing, snowmelt, albedo change, and temperature response to assess this feedback.

Figure 6 depicts the northern hemisphere distribution of annual mean surface forcing from BC in snow for 1998. The top panel shows mean gridcell forcing, which depends on snow cover fraction. The bottom panel shows forcing averaged only over snow covered surface within each gridcell, irrespective of SCF, and averaged only when snow is present. This metric describes the quantity of energy added specifically to snowpack, providing some insight into how local snowpack evolution may be affected. However, because model snow depth is very low in regions of low snow spatial coverage, and because forcing is reduced with shallow snowpack because of the radiative influence of the underlying ground, the snow-only forcing is significantly underestimated in unresolved mountainous terrain that should have deep snowpack. This deficiency can also be gleaned by noting very low snow-only forcing in the southern-most regions of model snow cover, where Figure 5

depicts large annual mean BC concentrations. The largest forcing is over the Tibetan Plateau (30–40 $^{\circ}$ N, 80–100 $^{\circ}$ E), averaging 1.5 $W m^{-2}$ over all-land. Forcing over northeastern China and much of Eurasia becomes larger when considering snow-only forcing, as expected from large BC/snow concentrations (Figure 5) but modest snow cover fraction. During some spring months, snow-only forcing exceeds 10 and 20 $W m^{-2}$ over parts of eastern China and the Tibetan Plateau, respectively. Even though BC mixing ratios and albedo reductions are greater in northeastern China, forc-

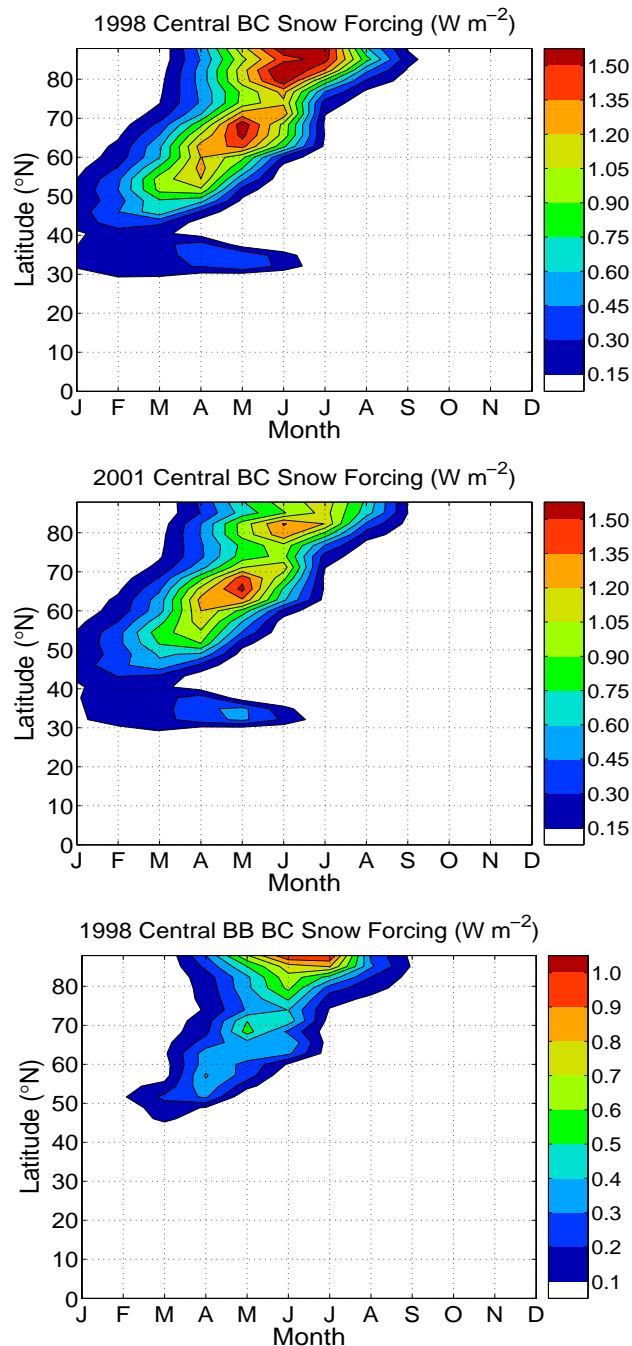


Figure 7. Zonal mean surface forcing from BC in snow as a function of month and latitude for (top) 1998 and (middle) 2001 central estimates, and (bottom) 1998 biomass burning only. The biomass burning forcing contribution is estimated as the difference between 1998 central (FF+BF+BB) and FF+BF only forcing.

ing is greater over the Tibetan Plateau because of greater ground-incident solar flux (because of closer proximity to the equator and less vegetation cover). More than 98% of the global forcing operates in the northern hemisphere.

Maximum BC/snow forcing occurs with the combination of high BC concentrations in snow, surface-incident solar flux, and snow cover. This pattern is manifested in Figure 7, which shows northern hemisphere zonal, monthly mean surface forcing from BC in snow for 1998 and 2001 central estimates and derived estimates of the 1998 biomass burning contribution. The latitude of maximum forcing moves north as the spring progresses, following regions with large amounts of snow and incident sunlight. While BC emissions are consistent or stronger in fall than spring (1998 boreal fire intensity peaked in August and September), seasonal snowpack does not generally form before incident sunlight significantly diminishes, thus greatly reducing forcing during the accumulation phase. 1998 arctic BC concentrations in snow peak in August, as opposed to July in 2001, attributable to boreal fires. But 80 – 90°N surface-incident solar flux drops to only 96 and 26 W m⁻² in August and September, reducing the radiative forcing potential. Thus April–June boreal fires have the greatest potential for strong BC/snow forcing. A second reason for greater forcing during the snow melt phase is accumulation of impurities near the surface. This effect is controlled by the scavenging ratio (Table 1), which is largely unconstrained.

The forcing space-time pattern in Figure 7 coincides closely with that of snowmelt onset. Thus, BC/snow forcing, while generally small, is maximum precisely when it can have the greatest influence on snowmelt rate. Zonal-mean forcing is large at

high-latitudes, even though BC concentrations are lower, because a greater portion of the surface is snow-covered. Arctic forcing is 17% greater in 1998 than 2001, and we attribute 35% of the total arctic forcing to biomass burning in 1998.

Strong evidence for BC influence on snowmelt timing is seen in Figure 8, which shows change in zonal mean snowmelt rate (averaged over land only), resulting from inclusion of BC in snow. Hatching shows statistically significant change at the 0.01 level. High latitude melt rate clearly increases during the early snowmelt phase and decreases during the late melt phase, as there is less snow available. Quantified one way, zonal mean melt rate increases in the experiments by 8 – 54% in the month prior to maximum melt of the controls at latitudes north of 50°N. Area-weighted, this increase is 28% and 19% for 1998 and 2001, respectively. Figure 8 shows that statistically significant melt changes are more widespread in 1998 than 2001.

Surface snowmelt on Greenland has been shown to increase the rate of ice-sheet flow [?]. Summer mean melt rate averaged over Greenland is 3% and 13% greater in 1998 and 2001 central experiments than their respective controls, but these changes are not significant at the 0.05 level. Summer T_{2m} warming over Greenland is 0.44 °C in both central experiments. Corresponding warming in both 1998 and 2001 high experiments is 1.15 °C, and melt rate changes are both significant at the 0.05 level. Central and high estimates of BC in Antarctic snow are too low to have significant influence on snow albedo, but we wonder if strong Australian wildfires could have a noticeable effect.

Along with snowmelt changes are highly significant reductions in zonal mean surface albedo. Figure 9 shows these changes, averaged over land and ocean, with hatching again at 0.01 significance.

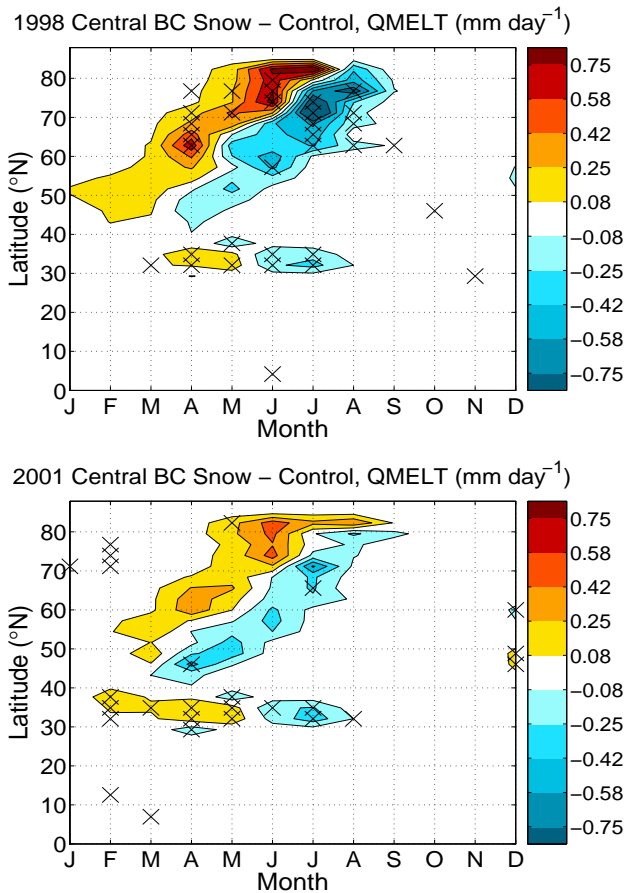


Figure 8. Difference in zonal monthly mean land snowmelt rate between central experiments and their respective controls. Experiment and control are identical except that BC only affects snow reflectance and heating in the experiment. Hatching shows statistically significant change at the 0.01 level.

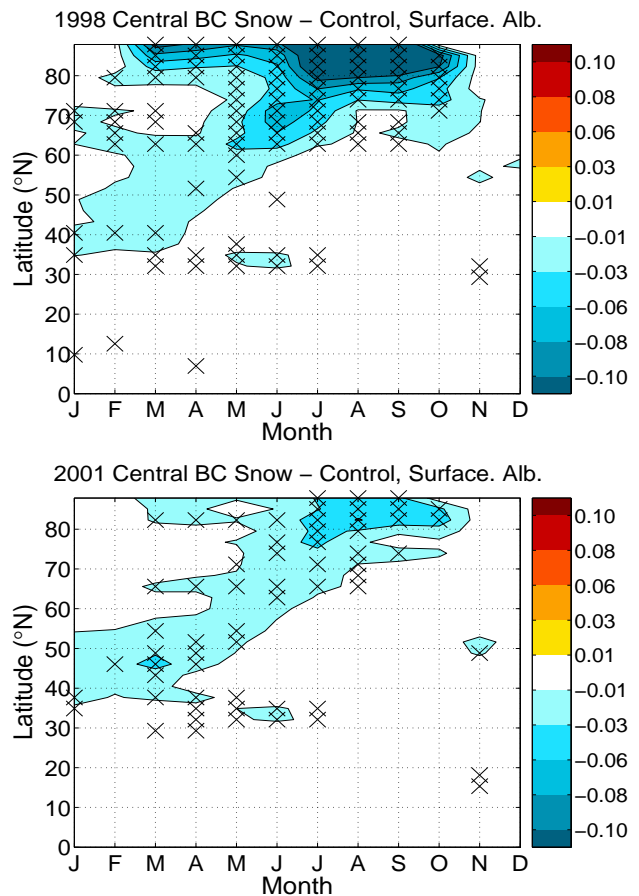


Figure 9. Difference in zonal monthly mean surface albedo between central BC/snow experiments and their respective controls. Hatching shows statistically significant change at the 0.01 level.

Annual mean albedo (weighted by surface insolation) of all arctic surface is reduced by 0.047 and 0.017 in 1998 and 2001 central experiments, respectively. The late-summer (August–September) 0.10 – 0.18 reduction in 80 – 90°N 1998 albedo happens because summer snow depth on sea-ice is reduced by 72%, exposing the darker bare sea-ice. This large reduction follows the 1.5 W m^{-2} June–July BC/snow forcing (Figure 7).

Observations spanning 1954–1991 from Soviet drifting stations indicate that snow on top of perennial sea-ice is generally nearly gone by July or August [?]. SHEBA observations from 1998 show snow ablation by early July [?], whereas model snow depth reaches August minimums of 29 and 13 cm in 1998 and 2001 central control simulations, respectively, and 5 and 11 cm in 1998 and 2001 central experiments. These observations indicate a model tendency of excessive snow cover on late-summer sea-ice. Perhaps encouragingly, the inclusion of BC in snow reduces model snow depth.

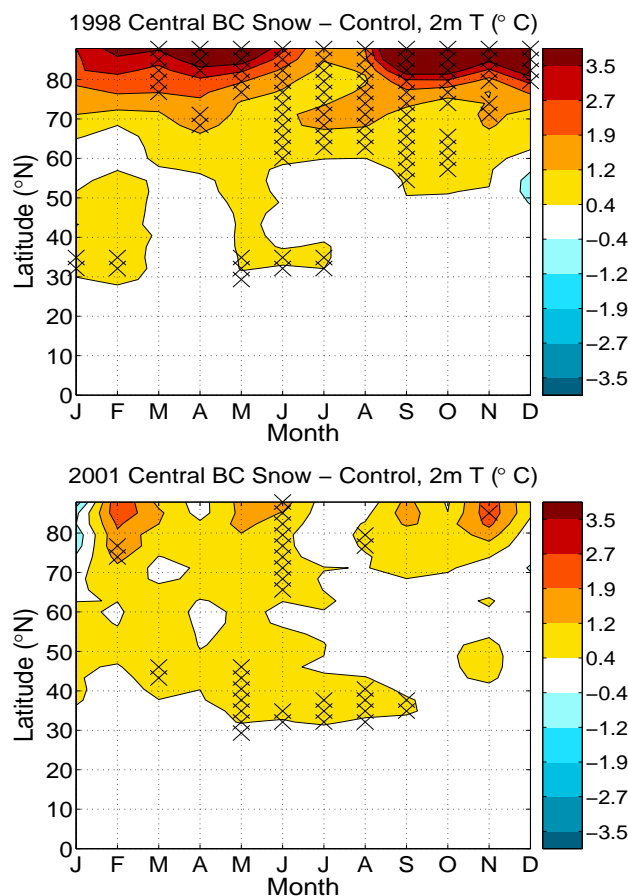


Figure 10. Difference in zonal monthly mean 2-meter air temperature between central BC/snow experiments and their respective controls. Hatching shows statistically significant change at the 0.01 level.

Table 4. Estimated Range of Change in Global Mean BC/Snow Radiative Forcing ($F_{s,snow}$), Represented as a Scalar, Resulting from Variation of Individual Factors. The Range is Relative to 1998 Central Estimates, Using Low and High Estimates of Each Factor in Table 1.

	Low	High
BC Emissions	0.54	2.00
Snow Aging	0.58	1.58
Melt Scavenging	0.69	1.08
Optical Properties	0.88	1.12
Snow Cover Fraction	0.83	1.08

Excess snowpack heating and climate feedback in the model also appear to accelerate snow grain growth, which darkens the snow itself and enhances the perturbation from BC (Figure 3). The increase in 80 – 90°N June and July r_e relative to 1998 central control is $289 \mu\text{m}$. The forcing responsible for this feedback is largely from biomass burning and is clearly damped in the 2001 central experiment (Figure 7), where 80 – 90°N June and July r_e is only $52 \mu\text{m}$ greater than 2001 central control, summer snow depth on sea-ice reduced by only 13%, and late-summer albedo reduced by 0.05. Note that these results are sensitive to the CSIM snow height/SCF relationship [?], which determines the proportion of exposed bare sea-ice. Slight changes to snow depths less than 10 cm have large impact on SCF and therefore albedo. In spite of large albedo reduction, sea-ice area changes are small. July–September mean arctic (66.5 – 90°N) sea-ice coverage is reduced by 3% and 1% in these two experiments relative to their respective control simulations.

Finally, Figure 10 shows significant surface air warming from BC in snow, especially from 60 – 90°N during June–November, 1998. Annual mean T_{2m} warming averaged over the Arctic is $+1.61$ and $+0.50^\circ\text{C}$ for 1998 and 2001. The late-summer polar warming pattern in 1998 is logically coupled with the forcing and albedo change patterns described above. 1998 winter and spring warming may be a consequence of thermal inertia from fall warming, or could be dynamical in nature. We note that our 1998 central experiment showed the highest efficacy of all experiments, so we urge caution in assuming that the large responses discussed are due entirely to biomass burning emissions, which cause only a modest increase in forcing (Figure 7c).

These changes provide evidence that significant snow-albedo feedback occurs from BC in snow, even though its forcing is small. Reasons why BC and other aerosols can provoke disproportionately large responses include their ability to warm snow, either directly melting it or priming it for earlier melt, enhanced snow grain metamorphism, which darkens the snow itself and increases the radiative perturbation by impurities, and amassing of impurities at the surface during melt. Changes in the timing of snow ablation, however, have the greatest influence on the surface energy balance because of the huge contrast in surface reflectance between snow and most other surfaces. Hence, the subtler effects of snow impurities come into play when they combine to influence snowmelt timing, as they apparently do in both 1998 and 2001 central experiments.

3.6. Individual Uncertainties

Finally, we examine the influence, to first order, that each of the five uncertainties discussed in Methods have individually on global snow/BC forcing. This offers insight into the relative importance of constraining uncertainty in each factor.

To derive estimates of variability in global annual mean $F_{s,snow}$, we performed the following experiments: For the role of BC emission scenarios, we conducted two 6-year simulations using 1998 central configuration (Table 1), but with low and high emissions estimates. For optical properties, we conducted offline 470-band SNICAR experiments, estimating hypothetical forcing assuming less-absorptive and more-absorptive BC, given annual-mean BC concentration and r_e at each gridcell of the 1998 central experiment. For snow aging, we also used offline SNICAR to estimate forcing at each gridcell, assuming annual mean BC concentration from the 1998 central experiment, but using the corresponding annual-mean r_e from the 1998 low and high experiments, representing slow and rapid aging. (If a gridcell contained snow in the central experiment, but not in the high or low, we assumed the global-mean high or low r_e). For the role of meltwater scavenging, we conducted another pair of 6-year CAM3 experiments with 1998 central configuration, but with meltwater scavenging factor ranging by two orders of magnitude (Table 1). Finally, we assess the role of SCF by scaling the BC/snow forcing at each gridcell of monthly output according to hypothetical SCF (calculated from snow depth), using the high and low representations discussed in Methods. Note that it would be more appropriate to estimate optical

property and aging uncertainty at monthly resolution, as with SCF, but this would require an excessive number of offline SNICAR runs.

The range in mean $F_{s,snow}$ estimated with these approaches is shown in Table 4. Uncertainty in emissions has the largest bearing on BC/snow forcing, closely followed by snow aging. The low–high range of FF+BF emissions from ? is greater than the range we derive for BB emissions (Table 1). Some of this difference is because we derive uncertainty using an observational inversion constraint, whereas uncertainty from ? is derived from compounding forward uncertainties. Global mean snow r_e varied from 91 – 812 μm between 1998 low and high experiments. While our choice of scaling snow aging by a factor of 2 was purely subjective, there are no observations of all relevant parameters required to constrain aging processes [?]. Uncertainty in scavenging factor can significantly decrease the global forcing estimate, but raise it only slightly. This happens because scavenging, even for hydrophilic impurities, is relatively inefficient in the central estimates. Thus decreasing the scavenging ratio increases the forcing only minimally in the high experiment, as impurities tend to reside near the surface during melt in the central experiment. Increasing the scavenging efficiency, however, significantly lowers the global forcing estimates, as impurities efficiently flush through the snowpack during the melt phase. ? report relatively uniform vertical profiles of BC in the snow on sea-ice during the SHEBA campaign in late March and April 1998. More observations of BC profiles during the melt phase will help constrain scavenging ratios. Additional offline SNICAR experiments showed that the range of effect of varying BC optical properties was relatively insensitive to snow grain size, in spite of the sensitivity of forcing to grain size (Figure 3), but the range narrowed slightly with increasing BC concentrations. Finally, the range of effect of SCF representation is small but slightly asymmetrical. This can be explained by the probability density function of snow depth where and when BC forcing operates. Snow depths greater than 20 cm predict SCF close to 1 with both central and high estimates, but much lower SCF with low estimates.

4. Conclusions

We incorporate our SNICAR model into the NCAR CAM3 GCM to improve quantification of present-day forcing, climate response, and associated uncertainties from black carbon (BC) in snow. This is the first global climate study which treats coupled snow aerosol heating and snow aging. We assemble model scenarios which bound the plausible range of present-day BC/snow forcing using combinations of BC emissions, BC optical properties, snow aging, meltwater scavenging of BC, and snow cover fraction. We estimate global annual mean BC/snow surface radiative forcings from all BC sources of +0.054 (0.007 – 0.13) and +0.049 (0.007 – 0.12) W m^{-2} during strong (1998) and weak (2001) boreal fire years, respectively. The forcing contributions from only fossil fuel+biofuel and only fossil fuel sources are +0.043 and +0.033 W m^{-2} , respectively. Central estimate predictions of BC

concentrations in snow capture the nearly 4 orders of magnitude range in observations with no apparent systematic bias, lending some confidence to our central forcing estimates. However, uncertainty in BC emissions and snow aging can individually account for a nearly two-fold range in forward-modeled global forcing. Uncertainty arising from the other factors is of order 20%.

Global annual mean equilibrium warming resulting from the inclusion of BC in snow is 0.15 and 0.10 $^{\circ}\text{C}$ for 1998 and 2001 central experiments, respectively. Annual arctic (66.5 – 90 $^{\circ}\text{N}$) warming, however, is 1.61 and 0.50 $^{\circ}\text{C}$. Arctic annual mean surface albedo for these two experiments is reduced by 0.047 and 0.017, relative to their control simulations without BC in snow. 1998 and 2001 land snowmelt rates north of 50 $^{\circ}\text{N}$ are 28% and 19% greater in the month preceding maximum melt of control simulations. These statistically significant climate signals all indicate that snow-albedo feedback is triggered by present-day BC/snow forcing. Greater climate response in 1998 might be attributable to strong boreal fires, which increase arctic BC/snow forcing by 17% relative to 2001. Climate response in our 1998 central experiment was unusually strong, however, and more simulations are needed to test this hypothesis. 1998 boreal fire strength peaked in August and September, whereas fires occurring in April–June have the greatest BC/snow forcing potential because of strong high-latitude insolation and large snow areal coverage. Even in the strong boreal fire year, we attribute 80% of the global BC/snow forcing to fossil fuel and biofuel sources.

Mean efficacy [?] of our 5 experiments is 3.17(2.1 – 4.5). This mean closely matches efficacy obtained from a long experiment with 10 \times present-day BC emissions, likely providing a more realistic efficacy estimate because of large temperature response relative to natural variability. BC in snowpack can provoke disproportionately large springtime climate response because the forcing tends to coincide with the onset of snowmelt, thus triggering more rapid snow ablation and snow-albedo feedback. The model and methods we develop here could be applied to study snow forcing by other aerosols, including mineral dust, volcanic ash, brown carbon, and marine sediment in sea-ice [?]. Sparseness of snow impurity measurements and uncertainty in snow effective radius variability suggest that more ground measurements need to be made and remote-sensing techniques refined to constrain understanding of this phenomenon on a global scale.

Acknowledgments. We thank Steve Warren for insightful comments after reviewing our manuscript and providing the spectral albedo measurements for Figure 2. We also thank two anonymous reviewers for comments. We thank Tami Bond for providing advice and recent manuscripts on black carbon optical properties, Prasad Kasibhatla for providing carbon monoxide inversion factors, M. Andreae for providing updated fire emission factors, Tom Painter for the opportunity to observe and measure, first-hand, snow-impurity effects, and Dani Bundy and Mariana Vertenstein for advice on CAM/SNICAR coupling. Funding for this work was provided by NSF/NCAR SGER ATM-0503148 and NASA Earth System Science Fellowship NNG05GP30H. Computations supported by Earth System Modeling Facility NSF ATM-0321380.